

See discussions, stats, and author profiles for this publication at: <https://www.researchgate.net/publication/284205948>

# In Situ Study of Spinel Ferrite Nanocrystal Growth Using Liquid Cell TEM

ARTICLE *in* CHEMISTRY OF MATERIALS · NOVEMBER 2015

Impact Factor: 8.35 · DOI: 10.1021/acs.chemmater.5b03930

READS

77

## 8 AUTHORS, INCLUDING:



**Wen-I Liang**

University of California, Berkeley

33 PUBLICATIONS 320 CITATIONS

SEE PROFILE



**Xiaowei Zhang**

Lawrence Berkeley National Laboratory

17 PUBLICATIONS 26 CITATIONS

SEE PROFILE



**Chung-Hua Chiu**

National Chiao Tung University

16 PUBLICATIONS 119 CITATIONS

SEE PROFILE



**Haimei Zheng**

Lawrence Berkeley National Laboratory

59 PUBLICATIONS 2,165 CITATIONS

SEE PROFILE

# In Situ Study of Spinel Ferrite Nanocrystal Growth Using Liquid Cell Transmission Electron Microscopy

Wen-I Liang,<sup>†,‡</sup> Xiaowei Zhang,<sup>‡,§</sup> Karen Bustillo,<sup>||</sup> Chung-Hua Chiu,<sup>†,‡</sup> Wen-Wei Wu,<sup>†</sup> Jun Xu,<sup>§</sup> Ying-Hao Chu,<sup>\*,†,⊥</sup> and Haimei Zheng<sup>\*,‡,‡</sup>

<sup>†</sup>Department of Materials Science and Engineering, National Chiao Tung University, Hsinchu 300, Taiwan

<sup>‡</sup>Materials Science Division and <sup>||</sup>National Center for Electron Microscopy, Molecular Foundry, Lawrence Berkeley National Laboratory, Berkeley, California 94720, United States

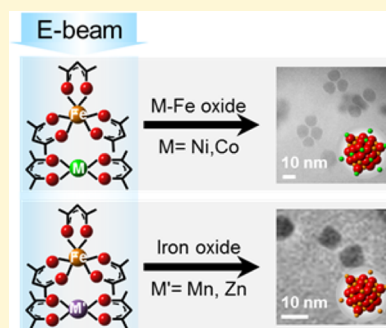
<sup>§</sup>National Laboratory of Solid State Microstructures, School of Electronic Science and Engineering, and Collaborative Innovation Centre of Advanced Microstructures, Nanjing University, Nanjing 210093, China

<sup>⊥</sup>Institute of Physics, Academia Sinica, Taipei 105, Taiwan

<sup>#</sup>Department of Materials Science and Engineering, University of California, Berkeley, California 94720 United States

## S Supporting Information

**ABSTRACT:** We report transition metal oxide nanocrystal formation in a liquid cell using transmission electron microscopy (TEM). The growth of M–Fe–oxide (M = Ni, Mn, Co, or Zn) nanoparticles from a growth solution of metal acetylacetonates dissolved in oleylamine, oleic acid, and benzyl ether was studied. Nickel iron oxide nanocrystals with spinel structure were obtained under electron beam irradiation of the Ni–Fe growth solution, whereas iron oxide nanocrystals were achieved with Mn remaining in the Mn–Fe growth solution. Similarly, we achieved cobalt iron oxide nanocrystals in the Co–Fe precursor solution, while iron oxide nanoparticles were obtained in the Zn–Fe solution. By tracking nanoparticle size evolution as a function of time along the Ni–Fe–oxide nanoparticle growth trajectories, we found the growth kinetics follow a Lifshitz–Slyozov–Wagner (LSW) model suggesting surface reaction-limited growth. Ex situ characterization shows elemental distribution and structural and valence state of the different nanoparticles. The trend of nanoparticle growth in a liquid cell shares many similarities with those in “one-pot” flask synthesis by thermal heating. We compare reduction potentials ( $E_r$ ) of the metal ions and thermal decomposition temperatures ( $T_d$ ) of the precursors and correlate them with nanoparticle growth in a liquid cell under TEM. We found a tendency to form mixed metal ion oxide nanoparticles instead of single metal ion (iron) oxides when the two precursors have similar values of  $T_d$  and metal ion reduction potential. The higher  $T_d$  and smaller  $E_r$  values of Mn and Zn precursors than those of Fe precursor, as well as Ni and Co precursors, may have resulted in the single metal ion (iron) oxide formation in M–Fe (M = Mn and Zn) precursor systems. This study sheds light on nanoparticle growth mechanisms by liquid cell TEM. In situ study of oxide nanocrystal growth using liquid cell TEM provides the opportunity to explore solution chemistry during nanocrystal growth beyond the nanoparticle growth that occurs in a TEM cell.

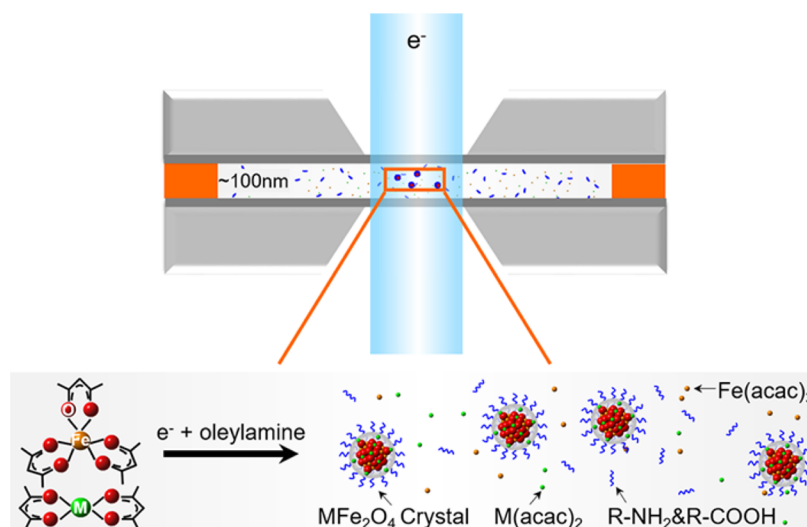


Functional oxide nanocrystals, such as spinel ferrites  $MFe_2O_4$ , where  $M(II) = Fe^{2+}, Mn^{2+}, Ni^{2+}, Zn^{2+},$  or  $Cu^{2+}$ , have attracted great interest due to their wide applications in biomedicine,<sup>1,2</sup> catalysis,<sup>3</sup> and high-density magnetic storage.<sup>4</sup> Over the past decade, a variety of methods has been developed to prepare ferrite nanocrystals, including coprecipitation, thermal decomposition, microemulsion, and hydrothermal synthesis,<sup>5</sup> among which the thermal decomposition method, using organic surfactants and solvents, has been highly successful in producing high-quality, monodisperse, and size-controllable nanocrystals. For example, it has been reported that thermal decomposition of iron(III) oleate precursor complexes produces large-scale monodisperse iron oxide nanocrystals with controllable size and shape.<sup>6</sup> It was also demonstrated that monodisperse  $Fe_3O_4$ ,<sup>7</sup>  $CoFe_2O_4$  and  $MnFe_2O_4$ <sup>8</sup> nanocrystals can be achieved by use of metal acetylacetonates (acac) as

precursor in the presence of 1,2-hexadecanediol, oleylamine, oleic acid, and phenol ether. This procedure has been widely adopted for synthesis of metal oxides.<sup>9</sup> Besides the synthesis achievements, understanding of nanocrystal formation mechanism is important.<sup>10</sup> It is generally believed that diols promote the reduction of an  $Fe^{3+}$  complex to obtain  $Fe_3O_4$ , which can be carried out with oleylamine as reducing agent and stabilizer<sup>11</sup> or with a mixture of oleic acid and oleylamine as the solvent.<sup>12</sup> Moreover, mechanisms have been postulated for the thermal decomposition of metal (acac) in the presence of primary amine.<sup>13</sup> In spite of significant efforts and speculations,<sup>14,15</sup> the formation mechanisms of nanocrystals and the effects of

Received: October 7, 2015

Revised: November 17, 2015



**Figure 1.** Illustration for spinel ferrite growth in liquid cell TEM.

surfactant/solvent on the structures of nanocrystals have yet to be thoroughly studied.

Liquid cell transmission electron microscopy (TEM)<sup>16–18</sup> provides an opportunity to monitor nanocrystal growth in situ, which can assist in elucidating the growth mechanisms of complex oxide nanocrystals. Many unseen mechanisms of colloidal nanocrystal growth have been discovered.<sup>18</sup> However, numerous previous studies have been on metals and alloys,<sup>19–23</sup> and there are only limited studies on oxides.<sup>24,25</sup> This is likely due to the complicated chemistry involving electron beam, precursor, and solvent. So far, the electron beam has been widely used to initiate the growth of nanocrystals in a liquid cell, mostly for convenience, although growth by thermal decomposition is possible.<sup>22,25</sup> In an aqueous solution, the electrolysis of water creates free radicals that reduce metallic precursors, initiating metal nanoparticle nucleation and growth. For example, spherical nanoparticles,<sup>23,26–28</sup> core–shell nanostructures,<sup>19,29,30</sup> nanowires,<sup>20,31</sup> and galvanic replacement of silver–palladium<sup>21</sup> have been achieved without the need to add additional reducing agents or to apply an external bias. There are also reports on the formation of semiconductor nanoparticles in aqueous solution by direct decomposition of the precursor solution under electron beam, such as the deposition of silicon,<sup>32</sup> PbS nanoparticle formation,<sup>33</sup> etc. In an organic solution, formation of metal and alloys can also be accomplished by electron beam reduction.<sup>20,34</sup> The formation mechanisms of metallic nanocrystals under electron beam have been explained by a radiochemical mechanism.<sup>35,36</sup> Little is known about the growth of metal oxide nanoparticles in a liquid cell under TEM.

In this study, we report the growth of transition metal oxide nanocrystals in organic solvent precursor solution by liquid cell TEM. We use Ni, Fe, Mn, Co, and Zn metal acetylacetonates, that is, Ni(acac)<sub>2</sub>, Fe(acac)<sub>3</sub>, Mn(acac)<sub>2</sub>, Co(acac)<sub>2</sub>, and Zn(acac)<sub>2</sub>, as the precursors and oleylamine (OAM), oleic acid, and benzyl ether as the surfactant and solvent, similar to the previously described study of ex situ colloidal synthesis of spinel ferrites.<sup>7,8</sup> Metal acetylacetonates are environmentally friendly and have low moisture sensitivity,<sup>37</sup> making them ideal for this study. Figure 1 illustrates the growth of complex oxide in a liquid cell.

## EXPERIMENTAL SECTION

**Material Growth.** The multicomponent system growth method was adopted from widely used thermal decomposition synthesis in organic solvents. The growth solution consisted of 0.1 mmol of M(acac)<sub>2</sub> (M = Ni, Mn, Co, or Zn) and 0.2 mmol of Fe(acac)<sub>3</sub> dissolved in 1 mL of surfactant/solvent (the ratio between oleylamine, oleic acid, and benzyl ether = 4.5:4.5:1). The sample solution was applied to both beam-induced growth and flask synthesis by the thermal decomposition method. In flask synthesis, all the mixed solutions were first heated to 60 °C, stirred at 600 rpm for 30 min, and then heated up to the designated temperature for a specific duration in the air as shown in Figure S4. After the reaction, the solution was cooled down to room temperature. One milliliter of ethanol was added and then the mixture was centrifuged to collect precipitates. These precipitates were washed two additional times by redispersing them in toluene and reprecipitating them by ethanol and centrifugation. All chemicals were purchased and used as received from Sigma–Aldrich Co.

**Liquid Cell Preparation.** We fabricated liquid cells by following our previously reported process.<sup>27</sup> Ultrathin silicon wafers (100 μm, 4-in., p-doped) purchased from Virginia Semiconductor (Fredericksburg, VA) were used. The fabrication of liquid cell was performed in the Marvell Nanofabrication Laboratory, University of California at Berkeley. We deposit a thin layer of SiN<sub>x</sub> membrane (10–15 nm) on both side of silicon wafer by low-pressure chemical vapor deposition (LPCVD). The fabrication is followed by lithography, wet KOH etching, spacer deposition, and liquid cell bonding. The gap between two silicon membranes of a liquid cell is defined by the thermodeposited indium layer, which is about 100 nm. After assembly of top and bottom cells, liquid cells are bonded and sealed with epoxy. The top two reservoirs remain open for liquid loading. Illustrations of the closed liquid cell can be found in previous studies.<sup>23,38</sup>

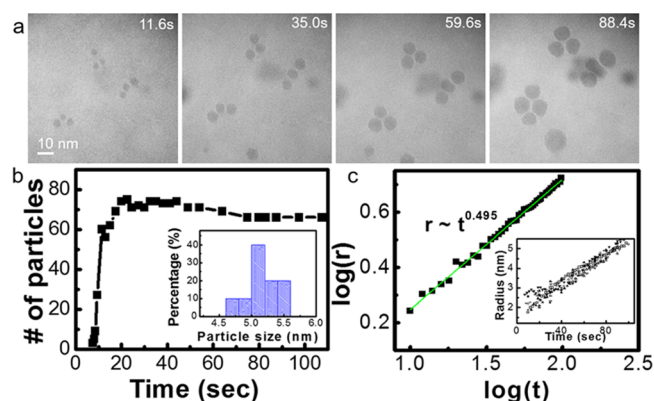
**In Situ Transmission Electron Microscopy Experiment.** For liquid cell growth experiments, about 100 nL of growth solution was loaded into a liquid cell by use of a syringe and Teflon tube. The top reservoirs were then sealed completely and loaded inside a TEM. Figure 1 shows a schematic of the reaction in a liquid cell. A JEOL 3010 TEM (with a LaB<sub>6</sub> cathode) operating at 300 kV was used, and an electron beam current density of ~10<sup>4</sup> A/m<sup>2</sup> was maintained during growth unless otherwise specified. Movies of the nanocrystal growth were captured at a rate of 10 frames/s by use of a Gatan Orius 833 camera and analyzed by use of ImageJ software.

**Transmission Electron Microscopic Characterization.** For characterization of as-grown and flask-synthesized nanocrystals, high-resolution (HR) TEM and electron energy-loss spectroscopy (EELS) were carried out on a FEI Tecnai F20 instrument equipped with a

Gatan image filter. HRTEM images were captured in the pristine liquid cell after it was air-dried for several days. To perform EELS measurements, the Gatan image filter was set with slit width of 20 eV, dispersion of 0.5 eV/pixel and zero-loss full width at half-maximum (FWHM) of  $\sim 0.7$  eV. Each spectrum was collected via point measurement for 1 s with the collection angle at 42 mrad. The spectral background was subtracted by DigitalMicrograph with a 20 eV window. In addition, a FEI Titan instrument at 200 kV with energy-dispersive X-ray mapping (EDS) ChemiSTEM capability was employed for elemental analysis. Prior to EDS mapping, the as-grown liquid cell samples were dried in an ambient environment for several days, and then they were opened in order to collect X-ray signals. The images were acquired in scanning tunneling electron microscopy (STEM) mode with a probe convergence semiangle ( $\alpha$ ) of 10 mrad. The beam current of 0.3 nA and pixel dwell times of 50–100  $\mu$ s were used. The mapping condition was kept constant in every experiment. Each EDS map was collected for no more than 60 s to minimize electron beam radiation damage. In addition, we used the Cliff–Lorimer method<sup>39</sup> provided by Espirit software to quantify the atomic percentage in each spectrum.

## RESULTS AND DISCUSSION

Figure 2a shows time-lapse images of nanocrystal growth from  $\text{Ni}(\text{acac})_2$  and  $\text{Fe}(\text{acac})_3$  precursor (also see Movie S1). Figure

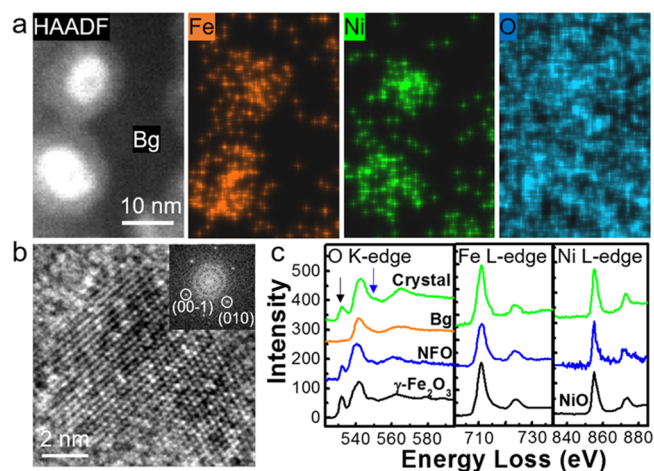


**Figure 2.** In situ observation and analysis of nanocrystal growth in a liquid cell from  $\text{Ni}(\text{acac})_2$  and  $\text{Fe}(\text{acac})_3$  precursors in the growth solution. (a) Image sequences of Ni–Fe–oxide nanocrystal growth. (b) Number of particles measured as a function of time. (Inset) Histogram showing size distribution of nanocrystals. The average radius is  $5.14 \pm 0.23$  nm. (c) Logarithmic relationship between particle radius and time. The green line is the linear fit. (Inset) Plot of nanoparticle growth trajectory as a function of time.

2b is a plot of the total number of particles observed within the viewing window as a function of time. The total number of particles was counted in a given area of about  $150 \times 150 \text{ nm}^2$ , and multiple areas of a single sample were analyzed. For some particles that drifted out of frame, they were not included after they disappeared from the viewing window, and minimum impact is expected due to the small fraction of such particles. As shown in the plot, the total number of particles increases rapidly and then reaches a plateau after  $\sim 30$  s. Such a growth process is similar to that in thermally activated flask synthesis.<sup>23</sup> It is noted that at the early stage particles move randomly, and they reach a stable stage at a later stage, where they tend to be immobilized either on the membrane or close to the adjacent particles due to van der Waals interactions. In addition, the size distribution of as-grown nanocrystals is shown in the inset of Figure 2b. The mean radius of nanoparticles is  $5.14 \pm 0.23$  nm.

To explore the growth kinetics, we track the changes of particle size as a function of time along their whole growth trajectories (Figure 2c). The growth trajectories of several particles are achieved and the growth kinetics fits well to power law behavior:  $r \sim t^\beta$ , where  $\beta$  is the growth exponent. The  $\beta$  value can be obtained by a linear fitting of the logarithmic relationship between particle radius and time, and  $\beta = 0.495 \pm 0.027$ , which suggests the surface reaction-limited growth of Lifshitz–Slyozov–Wagner (LSW) model ( $\beta = 0.5$ ).<sup>40</sup> This is consistent with the fact that the precursor concentration in this study is at least 2 times higher than that in traditional colloidal synthesis; thus the diffusion of ions is unlikely to be the detrimental step in particle growth but surface attachment of monomers is the limiting step. It is also noted that since the growth dynamics is strongly affected by many factors, including electron beam energy distribution, local precursor concentration, liquid cell geometry, etc., a difference between theoretically calculated and experimentally analyzed growth exponent is expected.<sup>24,41,42</sup>

To further understand the as-grown particles in the liquid cell, we performed further elemental characterization of the nanoparticles. Figure 3a shows EDS mapping of Ni–Fe–oxide



**Figure 3.** Characterization of as-grown nanocrystals in Ni–Fe–oxide system. (a) STEM–EDS technique shows (from left to right) HAADF image and corresponding iron, nickel, and oxygen maps. Maps shown here have been smoothed by convoluting a Gaussian function with a standard deviation of 3 pixels. (b) HR–TEM image and (inset) FFT indicate the nickel ferrite spinel structure with zone axis along the  $[100]$  direction. (c) STEM–EELS spectra of oxygen K-edge, iron L-edge, and nickel L-edge obtained from as-grown nanocrystal in a liquid cell (green, indicated in panel a), background (orange, indicated in panel a), thermally synthesized NFO nanocrystal (blue), and standard  $\gamma\text{-Fe}_2\text{O}_3$  and NiO crystals (black).

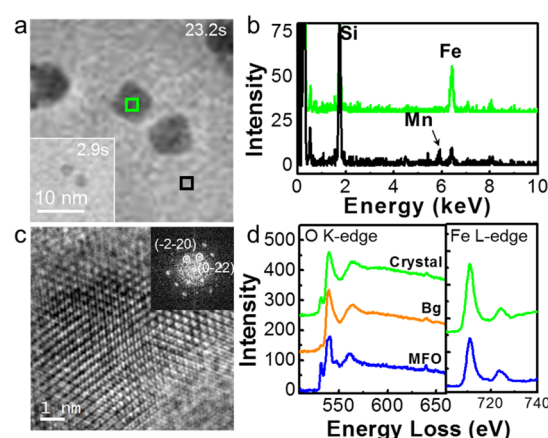
nanocrystals in the liquid cell. In a high-angle annular dark-field (HAADF) image, the contrast is attributed largely to thickness variation since Z numbers for Ni and Fe are similar. We observed a bright particle core surrounded by a light contrast shell. The iron map of a nanoparticle overlaps with the light contrast layer. Since we dried the liquid cell prior to ex situ characterization with STEM imaging, it is likely that amorphous iron oxide or iron hydroxide was formed during the drying process. The characteristic EDS spectra of nickel, iron, and oxygen are captured in a certain region that correlates with the HAADF image. Given the fact that a high concentration of oxygen is present in the organic solvents, the oxygen map does



not define the crystal shape as clearly as the other elements. A rough estimation indicates that the number of oxygen atoms in the residual solution per volume is only 1 order of magnitude smaller than that in a nanocrystal. Therefore, the shape of the nanocrystals in oxygen map is not as sharp as in the iron or nickel map (see detailed discussion in [Supporting Information](#)). Moreover, we sum up spectra from pixels in the crystal, integrate the area under the  $K_\alpha$  and  $K_\beta$  peaks, and use Cliff–Lorimer  $k$ -factor to calculate the composition ratio of the oxides. The results show that the ratio of Ni:Fe:O is about 0.57:1:1.9, confirming the formation of Ni–Fe–oxide compound (also see [Figure S1](#)). Additionally, the crystal structure is identified by high-resolution TEM. [Figure 3b](#) shows the lattice image and its fast Fourier transform (FFT). This image suggests that the crystal structure is spinel along the  $[100]$  zone axis. Combining the information from the EDS maps and HR-TEM image, we conclude that the as-grown crystal is close to  $\text{Ni}_x\text{Fe}_{3-x}\text{O}_4$  spinel structure.

In order to further verify the structure of as-grown nanoparticles, we conducted electron energy loss spectroscopy (EELS) experiments. [Figure 3c](#) shows EELS spectra from an as-grown crystal (green), background region (orange), nickel ferrite (NFO) synthesized ex situ by thermal activated method (blue), and standard reference spectra of  $\gamma\text{-Fe}_2\text{O}_3$  and NiO (black). From the EELS spectra, the presence of oxygen, iron, and nickel in the crystal can be confirmed. Second, the as-grown crystal has almost identical spectral features as the spectrum from NFO grown in flask synthesis. If we investigate the O K-edge closely (in the region 520–290 eV), the explicit prepeak (black arrow) of O K-edge in the nanocrystal, NFO, and  $\gamma\text{-Fe}_2\text{O}_3$  features hybridization of O 2p states with Fe 3d band, indicating metal oxide formation.<sup>43</sup> Moreover, a weak postpeak (blue arrow between 545 and 555 eV) appears in crystal, NFO, and  $\gamma\text{-Fe}_2\text{O}_3$ , exhibiting the character exclusively in  $\gamma\text{-Fe}_2\text{O}_3$  and  $\text{Fe}_3\text{O}_4$  system.<sup>44</sup> On the other hand, the background shows no prepeak nor postpeak feature as expected. Fe L-edge spectra (in the region 700–740 eV) of crystal, NFO, and  $\gamma\text{-Fe}_2\text{O}_3$  show similar features with  $\text{Fe}^{3+}$  valence state in  $\gamma\text{-Fe}_2\text{O}_3$ . Likewise, Ni L-edge spectra (in the region 835–885 eV) shows the typical shape of nickel oxide without ambiguity. Overall, we reach a conclusion that the as-grown nanocrystal is  $\text{Ni}_x\text{Fe}_{3-x}\text{O}_4$  with spinel structure on the basis of element analysis, phase identification and EELS study.

For comparison, we have studied nanocrystal growth in a liquid cell from  $\text{Mn}(\text{acac})_2$  and  $\text{Fe}(\text{acac})_3$  as precursors in the growth solution, where  $\text{Mn}^{2+}$  has a larger reduction potential (−1.18 V) and higher  $T_d$  (~250 °C) than those of  $\text{Ni}^{2+}$  and  $\text{Fe}^{3+}$ . Contrary to the system that forms the binary metal oxide from  $\text{Ni}(\text{acac})_2$  and  $\text{Fe}(\text{acac})_3$  precursors, pure iron oxide nanoparticles are achieved from  $\text{Mn}(\text{acac})_2$  and  $\text{Fe}(\text{acac})_3$  precursors (see growth of nanocrystals in [Movie S2](#) and characterization in [Figure 4](#)). [Figure 4a](#) shows the nanocrystals at different stages along the growth trajectory. A round nanoparticle at the early stage develops into a particle with facets at a later stage. [Figure 4b](#) shows EDS spectra integrated from a nanocrystal (green line and green box region in [Figure 4a](#)) and background (black line and black box region in [Figure 4a](#)). Mn signal is primarily found in the background surrounding the nanoparticle, whereas negligible Mn signal is detected in the nanoparticle region (also see [Figure S2](#) for EDS mapping). An as-grown nanocrystal is dominated by Fe and O signals. In addition to the EDS spectra, HR-TEM captures the lattice structure as shown in [Figure 4c](#), and a cubic structure can




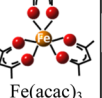
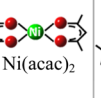
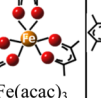
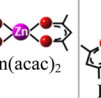
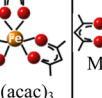
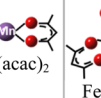
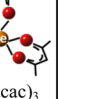
**Figure 4.** Characterization of as-grown nanocrystals in  $\text{Mn}(\text{acac})_2$  and  $\text{Fe}(\text{acac})_3$  precursors system. (a) Bright-field image at an early stage (left inset) and a later stage. (b) STEM–EDS spectra indicate the Fe K-edge and Mn K-edge signal from crystals (green box in panel a) and background (black box in panel a). (c) High-resolution image and FFT show the morphology and structure of crystals is close to FeO. (d) STEM–EELS spectra of oxygen K-edge and iron L-edge obtained from as-grown crystals (green), background in liquid cell (black), and thermally synthesized MFO crystals (blue).

be identified. We performed EELS analysis to examine the valence states of nanocrystal and background. We compare the O K-edge and Fe L-edge of the as-grown crystal in a liquid cell (green), background (Bg, orange), and ex situ manganese ferrite (MFO) synthesized by a thermal-activated method (blue). As shown in [Figure 4d](#), O K-edge (in the region 520–590 eV) and Fe L-edge (in the region 700–740 eV) show distinctive characteristics of iron oxide, while Mn L-edge (in the region 630–655 eV) lacks these clear features. This result supports the EDS results of in situ grown nanocrystals with negligible Mn. The existence of O prepeak around 532 eV for both in situ-grown nanocrystals and ex situ-synthesized MFO indicates iron oxide formation instead of iron metal. In addition, the fine structures of Fe L-edge, for both nanocrystal grown in situ and MFO grown by thermal decomposition, exhibit the same characteristics as the standard FeO spectrum.<sup>44</sup> Thus, we have inferred that the as-grown nanocrystal in the  $\text{Mn}(\text{acac})_2$  and  $\text{Fe}(\text{acac})_3$  precursor system belongs to FeO with a cubic structure. On the basis of these findings, we conclude that  $\text{Fe}(\text{acac})_3$  decomposes and forms iron oxide nanocrystals with a small amount of Mn, although both  $\text{Mn}(\text{acac})_2$  and  $\text{Fe}(\text{acac})_3$  are present in the solution.

Out of curiosity, we also investigated other spinel ferrite systems in the liquid cell, including the Co–Fe system [with  $\text{Co}(\text{acac})_2$  and  $\text{Fe}(\text{acac})_3$  precursors] and the Zn–Fe system [with  $\text{Zn}(\text{acac})_2$  and  $\text{Fe}(\text{acac})_3$  precursors]. The results show that cobalt iron oxide nanocrystals (with Co:Fe:O = 1.59:1:3.3) are achieved in the Co–Fe system, while iron oxide nanocrystals without Zn are formed in the Zn–Fe system. Detailed information can be found in [Supporting Information](#) ([Figure S3](#)).

[Table 1](#) summarizes the important parameters that have been considered in this study and lists major results. To understand why Ni–Fe and Co–Fe systems produce mixed metal oxides whereas Mn–Fe and Zn–Fe systems generate only iron oxide nanoparticles, several factors are discussed for possible precursor decomposition mechanisms. For instance, solvated electrons, local heating from the electron beam, and direct

Table 1. Summary of Important Parameters and Major Results in This Study<sup>a</sup>

	Co-Fe		Ni-Fe		Zn-Fe		Mn-Fe	
Precursor								
$E_r(M^{2+ \text{ or } 3+} \rightarrow M)$ (V) <sup>a</sup>	-0.28	-0.04	-0.25	-0.04	-0.76	-0.04	-1.18	-0.04
$T_d(^{\circ}\text{C})^b$	165	180	220	180	248	180	250	180
$\Delta T_d(^{\circ}\text{C})$	15		40		68		70	
Ternary oxide	Yes		Yes		No		No	
M <sup>c</sup> : Fe ratio	Co: Fe= 1.59: 1		Ni: Fe= 0.57: 1		Iron oxide		Iron oxide	

<sup>a</sup> $E_r$ , standard reduction potential of each metal ion. <sup>b</sup> $T_d$ , thermal decomposition temperature of precursors. <sup>c</sup>M = Co, Ni, Mn, or Zn.

bond cleavage can be important factors that influence nanocrystal growth. When the solvated electrons are considered, the reduction potential of the precursor ions may play a crucial role in the formation of either metal or metal oxide. As metal ions are reduced, it can be energetically favorable that transition metal nanoparticles would undergo the oxidation process easily. Moreover, in mixed Ni(acac)<sub>2</sub> and Fe(acac)<sub>3</sub> precursor solution, the reduction potentials are similar with  $-0.25$  V for  $\text{Ni}^{2+} \rightarrow \text{Ni}$  and  $-0.04$  V for  $\text{Fe}^{3+} \rightarrow \text{Fe}$ , while in the mixed Mn(acac)<sub>2</sub> and Fe(acac)<sub>3</sub> precursor solution, their reduction potential is very different with  $-1.18$  V for  $\text{Mn}^{2+} \rightarrow \text{Mn}$ . The reduction potential difference ( $\Delta E_r$ ) in these two systems might affect the final product as well. Second, the electron beam can introduce direct bond cleavage and thus decomposition of the precursor. However, it is unclear whether direct bond cleavage plays a dominant role in the nanoparticle formation (see the estimated energy in Table S2). Third, the electron beam-induced heating effect is also an important fact to consider. According to previous reports in solution chemistry, thermal decomposition of metal (acac) in a solution with primary amine could possibly introduce nanoparticle growth. In such oleylamine-assisted decomposition, oleylamine may start a nucleophilic attack on the carboxylic groups of the acetylacetonate ligand upon gaining energy and thus initiate crystal nucleation and growth.<sup>13</sup> The calculated temperature rise of the precursor solution under electron beam irradiation can be in a wide range in different scenarios. Although negligible temperature rise in a liquid cell is expected,<sup>23,45</sup> thermal effects might need to be re-evaluated when thermal conductivity of the liquid film is drastically reduced (Supporting Information). Future direct measurement of local temperature rise under the electron beam will be useful. Here, by applying the concept of chemical decomposition induced by heat from

ex situ flask synthesis, the precursor decomposition temperatures ( $T_d$ ) for Fe(acac)<sub>3</sub> ( $\sim 180$  °C), Ni(acac)<sub>2</sub> ( $\sim 220$  °C), and Mn(acac)<sub>2</sub> ( $\sim 250$  °C) may be useful indicators to determine the ease of decomposition.

A series of flask-synthesized Ni–Fe and Mn–Fe nanocrystals with different reaction temperatures and growth durations were therefore investigated in terms of morphology, structure, and composition (Figures S4 and S5). First of all, the morphology of nanocrystals grown by the flask method is different from those grown in the liquid cell. It is proposed that, in a TEM liquid cell, the thin cell geometry may confine the local reactions to two-dimensional growth, whereas in flask synthesis, growth can proceed in three dimensions and be relatively close to thermal equilibrium. Second, the reaction time and growth environment (static or vigorous stirring) do not affect the morphology or composition very much, while the reaction temperature appears to dictate chemical composition. Beginning with the Ni–Fe system, when the reaction temperature is as low as 80 °C, rod-shaped nanostructures have been identified as iron (oxyhydr)oxides by EDS and high-resolution TEM (Figure S5a).<sup>46</sup> When the reaction temperature reaches 150 °C, single-crystal nickel iron oxide (NFO) with spinel structure has formed (Figure S5b). The stoichiometry of Ni:Fe is close to 0.2:1, as determined by EDS. As we further increase the reaction temperature to 180 °C, Ni:Fe increases to 0.358:1, showing that chemical composition has strong dependence on reaction temperature. On the contrary, in the growth system with Mn(acac)<sub>2</sub> and Fe(acac)<sub>3</sub> precursors, the oxide composition shows a scarcity of Mn (Mn:Fe ratio <0.07:1) in this temperature range. These iron-rich oxide nanoparticles show good crystallinity and are identified as FeO structure (Figure S5c). Overall, element incorporation in flask synthesis also encounters difficulties in the Mn–Fe system but not the Ni–Fe

system in this temperature range. Similar results for flask synthesis have been demonstrated in other synthesis studies as well.<sup>47–50</sup> In conclusion, nanoparticles synthesized under electron beam in a liquid cell highly resemble those from thermal-activated synthesis in a lower temperature range.

## CONCLUSION

To summarize, we have systematically studied complex oxide growth in a liquid cell under TEM with a highly reductive environment. In the Ni–Fe system, growth of nickel iron oxide nanocrystal is achieved. However, in the Mn–Fe system, iron oxide is obtained while manganese remains in solution. Two possible formation routes are discussed: solvated electron-induced reduction process of transition metal ions and electron beam heating effect. We propose that incorporation of multiple components in the oxide nanostructures correlates with the difference in metal ion reduction potentials ( $\Delta E_r$ ) and thermal decomposition temperature ( $\Delta T_d$ ) of the precursors. For two precursors with smaller  $\Delta E_r$  and  $\Delta T_d$ , ternary oxides are formed, whereas for two precursors with larger  $\Delta E_r$  and  $\Delta T_d$ , single metal ion component oxide from the precursor with lower  $T_d$  and stronger  $E_r$  is formed. This trend applies to other systems, such as Co–Fe and Zn–Fe systems. Further estimation of temperature rise in the liquid cell using simplified model links us to low-temperature flask synthesis. We have discussed the resemblances and discrepancies between nanocrystals grown under the electron beam and those by thermally activated growth. The results may provide guidance for future synthesis of other transition metal oxides by liquid cell TEM. Future study is needed to decouple the effects imposed by the reduction potential and decomposition temperature.

## ASSOCIATED CONTENT

### Supporting Information

The Supporting Information is available free of charge on the ACS Publications website at DOI: 10.1021/acs.chemmater.5b03930.

Additional text, equations, and three tables describing estimation of oxygen concentration in an opened liquid cell, growth of nanocrystals in Co–Fe and Zn–Fe systems, and estimation of electron beam-induced temperature rise; six figures showing EDS spectrum of nickel ferrite nanocrystal, EDS maps for nanocrystals grown in Mn–Fe system, EDS spectra of nanocrystals grown in Co–Fe and Zn–Fe systems, bright-field images and materials characterization for ex situ flask synthesis, and electron beam-induced temperature rise (PDF)

In situ TEM movie S1 (AVI)

In situ TEM movie S2 (AVI)

## AUTHOR INFORMATION

### Corresponding Authors

\*(Y.-H.C.) E-mail [yhc@nctu.edu.tw](mailto:yhc@nctu.edu.tw).

\*(H.Z.) E-mail [hzmzheng@lbl.gov](mailto:hzmzheng@lbl.gov).

### Notes

The authors declare no competing financial interest.

## ACKNOWLEDGMENTS

We used TEM facilities at the Molecular Foundry of Lawrence Berkeley National Laboratory, which is supported by the U.S. Department of Energy (DOE) under Contract DE-AC02-05CH11231. W.-I.L. and Y.-H.C. acknowledge funding support

from the Ministry of Science and Technology (MOST) in Taiwan (NSC 102-2119-I-009-502). X.Z. and J.X. acknowledge the support of National Basic Research Program of China (2013CB632101) and China Scholarship Council (201406190080). C.-H.C. acknowledges funding support from the Ministry of Science and Technology (MOST) in Taiwan (Grant 103-2917-I-009-185). This project was supported by U.S. DOE Office of Science Early Career Research Program under H.Z.

## REFERENCES

- (1) Kumar, C. S. S. R.; Mohammad, F. Magnetic nanomaterials for hyperthermia-based therapy and controlled drug delivery. *Adv. Drug Delivery Rev.* **2011**, *63*, 789–808.
- (2) Xie, J.; Liu, G.; Eden, H. S.; Ai, H.; Chen, X. Surface-Engineered Magnetic Nanoparticle Platforms for Cancer Imaging and Therapy. *Acc. Chem. Res.* **2011**, *44*, 883–892.
- (3) Polshettiwar, V.; Luque, R.; Fihri, A.; Zhu, H.; Bouhrara, M.; Basset, J.-M. Magnetically Recoverable Nanocatalysts. *Chem. Rev.* **2011**, *111*, 3036–3075.
- (4) Frey, N. A.; Peng, S.; Cheng, K.; Sun, S. Magnetic nanoparticles: synthesis, functionalization, and applications in bioimaging and magnetic energy storage. *Chem. Soc. Rev.* **2009**, *38*, 2532–2542.
- (5) Laurent, S.; Forge, D.; Port, M.; Roch, A.; Robic, C.; Vander Elst, L.; Muller, R. N. Magnetic Iron Oxide Nanoparticles: Synthesis, Stabilization, Vectorization, Physicochemical Characterizations, and Biological Applications. *Chem. Rev.* **2008**, *108*, 2064–2110.
- (6) Park, J.; An, K.; Hwang, Y.; Park, J.-G.; Noh, H.-J.; Kim, J.-Y.; Park, J.-H.; Hwang, N.-M.; Hyeon, T. Ultra-large-scale syntheses of monodisperse nanocrystals. *Nat. Mater.* **2004**, *3*, 891–895.
- (7) Sun, S.; Zeng, H. Size-Controlled Synthesis of Magnetite Nanoparticles. *J. Am. Chem. Soc.* **2002**, *124*, 8204–8205.
- (8) Sun, S.; Zeng, H.; Robinson, D. B.; Raoux, S.; Rice, P. M.; Wang, S. X.; Li, G. Monodisperse  $MFe_2O_4$  ( $M = Fe, Co, Mn$ ) Nanoparticles. *J. Am. Chem. Soc.* **2004**, *126*, 273–279.
- (9) Salas, G.; Costo, R.; Morales, M. P. Magnetic Nanoparticles. In *Nanobiotechnology: Inorganic Nanoparticles vs Organic Nanoparticles*; de la Fuente, J. M., Grazu, V., Eds.; Elsevier: Amsterdam, 2012.
- (10) Wang, F.; Richards, V. N.; Shields, S. P.; Buhro, W. E. Kinetics and Mechanisms of Aggregative Nanocrystal Growth. *Chem. Mater.* **2014**, *26*, 5–21.
- (11) Xu, Z.; Shen, C.; Hou, Y.; Gao, H.; Sun, S. Oleylamine as Both Reducing Agent and Stabilizer in a Facile Synthesis of Magnetite Nanoparticles. *Chem. Mater.* **2009**, *21*, 1778–1780.
- (12) Kikuchi, T.; Kasuya, R.; Endo, S.; Nakamura, A.; Takai, T.; Metzler-Nolte, N.; Tohji, K.; Balachandran, J. Preparation of magnetite aqueous dispersion for magnetic fluid hyperthermia. *J. Magn. Magn. Mater.* **2011**, *323*, 1216–1222.
- (13) Pinna, N.; Garnweitner, G.; Antonietti, M.; Niederberger, M. A General Nonaqueous Route to Binary Metal Oxide Nanocrystals Involving a C–C Bond Cleavage. *J. Am. Chem. Soc.* **2005**, *127*, 5608–5612.
- (14) Jana, N. R.; Chen, Y.; Peng, X. Size- and Shape-Controlled Magnetic (Cr, Mn, Fe, Co, Ni) Oxide Nanocrystals via a Simple and General Approach. *Chem. Mater.* **2004**, *16*, 3931–3935.
- (15) Harris, R. A.; Shumbula, P. M.; van der Walt, H. Analysis of the Interaction of Surfactants Oleic Acid and Oleylamine with Iron Oxide Nanoparticles through Molecular Mechanics Modeling. *Langmuir* **2015**, *31*, 3934–3943.
- (16) Zheng, H.; Meng, Y. S.; Zhu, Y. Frontiers of in situ electron microscopy. *MRS Bull.* **2015**, *40*, 12–18.
- (17) Chen, X.; Li, C.; Cao, H. Recent developments of the in situ wet cell technology for transmission electron microscopies. *Nanoscale* **2015**, *7*, 4811–4819.
- (18) Liao, H.-G.; Niu, K.; Zheng, H. Observation of growth of metal nanoparticles. *Chem. Commun.* **2013**, *49*, 11720–11727.
- (19) Jungjohann, K. L.; Bliznakov, S.; Sutter, P. W.; Stach, E. A.; Sutter, E. A. In Situ Liquid Cell Electron Microscopy of the Solution



Growth of Au–Pd Core–Shell Nanostructures. *Nano Lett.* **2013**, *13*, 2964–2970.

(20) Liao, H.-G.; Cui, L.; Whitlam, S.; Zheng, H. Real-Time Imaging of Pt3Fe Nanorod Growth in Solution. *Science* **2012**, *336*, 1011–1014.

(21) Sutter, E.; Jungjohann, K.; Bliznakov, S.; Courty, A.; Maisonnaite, E.; Tenney, S.; Sutter, P. In situ liquid-cell electron microscopy of silver–palladium galvanic replacement reactions on silver nanoparticles. *Nat. Commun.* **2014**, *5*, No. 4946, DOI: 10.1038/ncomms5946.

(22) Xin, H. L.; Zheng, H. In Situ Observation of Oscillatory Growth of Bismuth Nanoparticles. *Nano Lett.* **2012**, *12*, 1470–1474.

(23) Zheng, H.; Smith, R. K.; Jun, Y.-w.; Kisielowski, C.; Dahmen, U.; Alivisatos, A. P. Observation of Single Colloidal Platinum Nanocrystal Growth Trajectories. *Science* **2009**, *324*, 1309–1312.

(24) Liu, Y.; Tai, K.; Dillon, S. J. Growth Kinetics and Morphological Evolution of ZnO Precipitated from Solution. *Chem. Mater.* **2013**, *25*, 2927–2933.

(25) Niu, K.-Y.; Park, J.; Zheng, H.; Alivisatos, A. P. Revealing Bismuth Oxide Hollow Nanoparticle Formation by the Kirkendall Effect. *Nano Lett.* **2013**, *13*, 5715–5719.

(26) Noh, K. W.; Liu, Y.; Sun, L.; Dillon, S. J. Challenges associated with in-situ TEM in environmental systems: The case of silver in aqueous solutions. *Ultramicroscopy* **2012**, *116*, 34–38.

(27) Liao, H.-G.; Zherebetskyy, D.; Xin, H.; Czarnik, C.; Ercius, P.; Elmlund, H.; Pan, M.; Wang, L.-W.; Zheng, H. Facet development during platinum nanocube growth. *Science* **2014**, *345*, 916–919.

(28) Parent, L. R.; Robinson, D. B.; Woehl, T. J.; Ristenpart, W. D.; Evans, J. E.; Browning, N. D.; Arslan, I. Direct in Situ Observation of Nanoparticle Synthesis in a Liquid Crystal Surfactant Template. *ACS Nano* **2012**, *6*, 3589–3596.

(29) Sutter, E. A.; Sutter, P. W. Determination of Redox Reaction Rates and Orders by In Situ Liquid Cell Electron Microscopy of Pd and Au Solution Growth. *J. Am. Chem. Soc.* **2014**, *136*, 16865–16870.

(30) Wu, J.; Gao, W.; Wen, J.; Miller, D. J.; Lu, P.; Zuo, J.-M.; Yang, H. Growth of Au on Pt Icosahedral Nanoparticles Revealed by Low-Dose In Situ TEM. *Nano Lett.* **2015**, *15*, 2711–2715.

(31) Kraus, T.; de Jonge, N. Dendritic Gold Nanowire Growth Observed in Liquid with Transmission Electron Microscopy. *Langmuir* **2013**, *29*, 8427–8432.

(32) Liu, Y.; Chen, X.; Noh, K. W.; Dillon, S. J. Electron beam induced deposition of silicon nanostructures from a liquid phase precursor. *Nanotechnology* **2012**, *23*, No. 385302.

(33) Evans, J. E.; Jungjohann, K. L.; Browning, N. D.; Arslan, I. Controlled Growth of Nanoparticles from Solution with In Situ Liquid Transmission Electron Microscopy. *Nano Lett.* **2011**, *11*, 2809–2813.

(34) Liao, H.-G.; Zheng, H. Liquid Cell Transmission Electron Microscopy Study of Platinum Iron Nanocrystal Growth and Shape Evolution. *J. Am. Chem. Soc.* **2013**, *135*, 5038–5043.

(35) Woehl, T. J.; Jungjohann, K. L.; Evans, J. E.; Arslan, I.; Ristenpart, W. D.; Browning, N. D. Experimental procedures to mitigate electron beam induced artifacts during in situ fluid imaging of nanomaterials. *Ultramicroscopy* **2013**, *127*, 53–63.

(36) Woehl, T. J.; Evans, J. E.; Arslan, I.; Ristenpart, W. D.; Browning, N. D. Direct in Situ Determination of the Mechanisms Controlling Nanoparticle Nucleation and Growth. *ACS Nano* **2012**, *6*, 8599–8610.

(37) Willis, A. L.; Chen, Z.; He, J.; Zhu, Y.; Turro, N. J.; O'Brien, S. Metal Acetylacetonates as General Precursors for the Synthesis of Early Transition Metal Oxide Nanomaterials. *J. Nanomater.* **2007**, *2007*, 14858.

(38) Zheng, H. Using molecular tweezers to move and image nanoparticles. *Nanoscale* **2013**, *5*, 4070–4078.

(39) Cliff, G.; Lorimer, G. W. The quantitative analysis of thin specimens. *J. Microsc.* **1975**, *103*, 203–207.

(40) Lifshitz, I. M.; Slyozov, V. V. The kinetics of precipitation from supersaturated solid solutions. *J. Phys. Chem. Solids* **1961**, *19*, 35–50.

(41) Bhattacharya, D.; Bosman, M.; Mokkapatil, V. R. S. S.; Leong, F. Y.; Mirsaidov, U. Nucleation Dynamics of Water Nanodroplets. *Microsc. Microanal.* **2014**, *20*, 407–415.

(42) Woehl, T. J.; Park, C.; Evans, J. E.; Arslan, I.; Ristenpart, W. D.; Browning, N. D. Direct Observation of Aggregative Nanoparticle Growth: Kinetic Modeling of the Size Distribution and Growth Rate. *Nano Lett.* **2014**, *14*, 373–378.

(43) Lafuerza, S.; Subías, G.; García, J.; Di Matteo, S.; Blasco, J.; Cuartero, V.; Natoli, C. R. Origin of the pre-peak features in the oxygen K-edge x-ray absorption spectra of LaFeO<sub>3</sub> and LaMnO<sub>3</sub> studied by Ga substitution of the transition metal ion. *J. Phys.: Condens. Matter* **2011**, *23*, No. 325601.

(44) Colliex, C.; Manoubi, T.; Ortiz, C. Electron-energy-loss-spectroscopy near-edge fine structures in the iron-oxygen system. *Phys. Rev. B: Condens. Matter Mater. Phys.* **1991**, *44*, 11402–11411.

(45) Zheng, H.; Claridge, S. A.; Minor, A. M.; Alivisatos, A. P.; Dahmen, U. Nanocrystal Diffusion in a Liquid Thin Film Observed by in Situ Transmission Electron Microscopy. *Nano Lett.* **2009**, *9*, 2460–2465.

(46) Frandsen, C.; Legg, B. A.; Comolli, L. R.; Zhang, H.; Gilbert, B.; Johnson, E.; Banfield, J. F. Aggregation-induced growth and transformation of  $\beta$ -FeOOH nanorods to micron-sized [small alpha]-Fe<sub>2</sub>O<sub>3</sub> spindles. *CrystEngComm* **2014**, *16*, 1451–1458.

(47) Kang, Y.; Pyo, J. B.; Ye, X.; Gordon, T. R.; Murray, C. B. Synthesis, Shape Control, and Methanol Electro-oxidation Properties of Pt–Zn Alloy and Pt<sub>3</sub>Zn Intermetallic Nanocrystals. *ACS Nano* **2012**, *6*, 5642–5647.

(48) Yu, Y.; Yang, W.; Sun, X.; Zhu, W.; Li, X. Z.; Sellmyer, D. J.; Sun, S. Monodisperse MPt (M = Fe, Co, Ni, Cu, Zn) Nanoparticles Prepared from a Facile Oleylamine Reduction of Metal Salts. *Nano Lett.* **2014**, *14*, 2778–2782.

(49) Ye, X.; Collins, J. E.; Kang, Y.; Chen, J.; Chen, D. T. N.; Yodh, A. G.; Murray, C. B. Morphologically controlled synthesis of colloidal upconversion nanophosphors and their shape-directed self-assembly. *Proc. Natl. Acad. Sci. U. S. A.* **2010**, *107*, 22430–22435.

(50) Bao, N.; Shen, L.; An, W.; Padhan, P.; Heath Turner, C.; Gupta, A. Formation Mechanism and Shape Control of Monodisperse Magnetic CoFe<sub>2</sub>O<sub>4</sub> Nanocrystals. *Chem. Mater.* **2009**, *21*, 3458–3468.